73rd International Astronautical Congress (IAC), Paris, France, 18-22 Semptember 2022.

IAC-22,C1,9,10,x73057

An algorithm to engineer autonomous ballistic capture at Mars

Gianmario Merisio[1], and **Francesco Topputo**[2].

Current deep-space missions heavily count on ground-based operations. Although reliable, ground slots will saturate soon, so hampering the current momentum in space exploration. EXTREMA, a project awarded an ERC Consolidator Grant in 2019, enables self-driving spacecraft, challenging the current paradigm and aiming, among others, at autonomously engineering ballistic capture. This work presents an autonomous ballistic capture algorithm suitable for spacecraft with limited control authority and onboard resources. The algorithm is applied to construct BC corridors at Mars, time-varying manifolds supporting capture that can be targeted far away from the planet. The algorithm envisaged a novel methodology to generate families of ballistic capture orbits characterized by succeeding capture epochs. The families are built by correcting in sequence the initial conditions of ballistic capture orbits provided that they are enough regular. New orbits are obtained solving a well-posed three-point boundary value problem exhibiting 8 boundary conditions. The conditions are linearized, and the problem is solved for a finite set of variables with the multiple shooting technique. The computationally demanding problem of finding ballistic capture orbits through stable sets manipulation is unburdened by just solving a linear system, making the algorithm compatible with CubeSats onboard resources. An overview of the autonomous BC algorithm and the details of the correction procedure are provided. The methodology is applied to generate families of orbits belonging to capture sets $\mathcal{C}^1_{-1}$ and $\mathcal{C}^6_{-1}$ starting from the same baseline capture orbit. In both cases, the method constructs sequences of initial conditions spanning more than 100 days. The algorithm performance is assessed and its limitations are discussed. Results are inspected against the solar gravity gradient field to get insight about how the methodology acts when it corrects a reference solution into a new capture orbit.

1 Introduction

The space sector is experiencing flourishing growth and evidence is mounting that the near future will be characterized by a large amount of deep-space missions [1–3]. In the last decade, CubeSats have granted affordable access to space due to their reduced manufacturing costs compared to traditional missions. At the present-day, most miniaturized spacecraft has thus far been deployed into near-Earth orbits, but soon a multitude of interplanetary CubeSats will be employed for deep-space missions as well. However, the current paradigm for deep-space missions strongly relies on ground-based operations. Although reliable, this approach will rapidly cause saturation of ground slots, hampering the current momentum in space exploration.

EXTREMA (short for *Engineering Extremely Rare Events in Astrodynamics for Deep-Space Missions in Autonomy*) enables self-driving spacecraft, challenging the current paradigm under which spacecraft are piloted in the interplanetary space [4, 5]. Deep-space guidance, navigation, and control (GNC) applied in a complex scenario is the subject of EXTREMA, which aims, among others, to engineer ballistic capture (BC) in a totally autonomous fashion [6, 7]. EXTREMA is erected on three pillars. Pillar 1 is about autonomous navigation [8–10]. Pillar 2 involves autonomous guidance and control [11, 12]. Pillar 3 deals with autonomous ballistic capture (ABC), the focus of this work. The project has been awarded a European Research Council (ERC) Consolidator Grant in 2019.

BC orbits are low-energy transfers that allow temporary capture about a planet exploiting the natural dynamics, thus without requiring maneuvers [13]. Compared to Keplerian solutions, they are cheaper, safer, and more versatile from the operational perspective at the expense of longer transfer times. BC orbits are bounded by the weak stability boundary (WSB) [13–16]. After being initially conceived as a fuzzy boundary region in the Sun–Earth–Moon system [17, 18], the WSB was algorithmically defined in [19]. The definition was later extended in [20–22]. A formal definition and a technique for its derivation were proposed in [23]. To date, despite the effort put in numerous works [20, 24–27], both WSB and BC are still not completely understood. Nonetheless, a connection between celestial and quantum mechanics was recently found exploiting the WSB [28], providing a fresh perspective to tackle the problem.

Currently, two approaches are known for designing

[1]PhD Student, Department of Aerospace Science and Technology, Politecnico di Milano, Via La Masa 34, 20156, Milano, Italy, gianmario.merisio@polimi.it
[2]Full Professor, Department of Aerospace Science and Technology, Politecnico di Milano, Via La Masa 34, 20156, Milano, Italy; francesco.topputo@polimi.it

BC orbits: the technique stemmed from invariant manifolds [26, 29], and the method based on stable sets manipulation [23, 30]. The former gives insights into the dynamics but its application is limited to autonomous systems (e. g., the circular restricted 3-body problem), while the latter can be applied to more representative, non-autonomous models, although being computationally expensive [21, 31]. Lately, the variational theory for Lagrangian coherent structures [32, 33], and the Taylor differential algebra [34] were applied to derive BC orbits and the WSB more efficiently [35, 36].

An overview of the ABC algorithm is provided. However, the primary goal of this work is to present a novel methodology devised to generate families of BC orbits characterized by succeeding capture epochs. The problem of finding a new capture orbit at the desired capture epoch correcting a known reference solution is stated. Effort is put in making the method suitable for autonomous spacecraft with limited onboard resources (e. g., CubeSats). The flow expansion applied to tackle the problem is discussed. The necessary boundary conditions are explained individually. To compute new orbits, a three-point boundary value problem (3PBVP) with linearized boundary conditions is solved with the multiple shooting technique. Expanding the flow and linearizing boundary conditions reduce the problem to the solution of a linear system. Applying the multiple shooting technique decreases the problem sensitivity. Families are computed correcting in sequence the initial conditions of enough regular ballistic capture orbits. The algorithm is applied to generate families of capture orbits belonging to $\mathcal{C}^1_{-1}$ and $\mathcal{C}^6_{-1}$. Sequences of BC orbits are computed starting from a baseline orbit selected for its remarkable regularity. Performance and limitations of the algorithm are discussed too. Finally, results are inspected against streamlines of the solar gravity gradient in an effort to reveal the nature of the corrections applied on the reference capture orbits.

The remainder of the paper is organized as follows. In Section 2, the BC mechanism and the dynamical model are introduced. Then, the methodology follows in Section 3. Results are presented and discussed in Section 4. Eventually, conclusions are drawn in Section 5.

2 Background

2.1 Ballistic capture mechanism

BC orbits are characterized by initial conditions (ICs) escaping the target when integrated backward and performing n revolutions about it when propagated forward, neither impacting nor escaping the target. In forward time, particles flying on BC orbits approach the target coming from outside its sphere of influence (SOI) and remain temporarily captured about it. After a certain time, the particle escapes if an energy dissipation mechanism does not take place to make the capture permanent. To dissipate energy either a breaking maneuver or the target's atmosphere (if available) could be used [37, 38].

When searching for BC opportunities, most of the trajectories found are spurious solutions which are typically not useful for mission design purposes [30]. Useful solutions are detected exploiting the regularity index[1] S and regularity coefficient $\Delta S_{\%}$ [40]. The aim is seeking for ideal orbits that presents regular post-capture legs resulting in n revolutions about the target which are similar in orientation and shape. Numerical experiments showed that high-quality post-capture orbits are identified by small regularity index and coefficient [30, 31, 39, 40]. If the regularity index and coefficient are indicators used to qualitatively judge post-capture legs, capture occurrence is quantitatively measured through the capture ratio $\mathcal{R}_{\mathcal{C}}$ [31]. Typically, search spaces characterized by larger capture ratio are desirable when looking for BC orbits.

A particle stability is inferred using a plane in the three-dimensional physical space [14], according to the spatial stability definition provided in [30]. Based on its dynamical behavior, a trajectory is classified as:

i) *weakly stable* (sub-set $\mathcal{W}_i$) if the particle performs i complete revolutions around the target neither escaping nor impacting with it or its moons;

ii) *unstable* (sub-set $\mathcal{X}_i$) if the particle escapes from the target before completing the i-th revolution;

iii) *crash* (sub-set $\mathcal{K}_i$) if the particle impacts the with target before completing the i-th revolution;

iv) *moon–crash* (sub-set $\mathcal{M}_i$) if the particle impacts with one of the target's moons before completing the i-th revolution;

v) *acrobatic* (sub-set $\mathcal{D}_i$) if none of the previous conditions occurs within the integration time span.

Conditions ii)-v) apply after the particle performs $(i-1)$ revolutions around the target. The sub-sets are defined for $i \in \mathbb{Z}\backslash\{0\}$, where the sign of i informs on the propagation direction. If $i > 0$ ($i < 0$), then the IC is propagated forward (backward) in time. A capture set is defined as $\mathcal{C}^n_{-1} := \mathcal{W}_n \cap \mathcal{X}_{-1}$. Therefore, it is the intersection between the weakly stable (also referred to as stable throughout the manuscript) set in forward time $\mathcal{W}_n$ and the unstable set in backward time $\mathcal{X}_{-1}$ [30].

[1] In previous works this was referred to as stability index [30, 31, 39]. However, in [40], the adjustment from *stability* to *regularity* index was proposed to avoid misunderstandings with the periodic orbit stability index. The same nomenclature introduced in [40] is used in this work.

2.2 Dynamical model

According to the nomenclature introduced in [30], a *target* (also referred to as *central body*) and a *primary* are defined. The target being the body around which the motion of the spacecraft is studied (Mars in this work), and the primary being the body around which the target revolves (the Sun). Target and primary masses are m_t and m_p, respectively.

2.2.1 Reference frames

In this work, the following reference frames are used: J2000, ECLIPJ2000, and RTN.

J2000. Defined on the Earth's mean equator and equinox, the J2000 is an inertial frame determined from observations of planetary motions that was realized to coincide almost exactly with the International Celestial Reference Frame (ICRF) [41]. Equations of motion (EoM) are integrated in this reference frame.

ECLIPJ2000. This is an inertial frame built-in in SPICE that is defined on the ecliptic coordinates and based on the J2000 inertial frame. The origin of the ECLIPJ2000 frame can be chosen arbitrarily.

RTN@t_i. The radial-tangential-normal of date frame (RTN) is an inertial frame frozen at a prescribed epoch t_i. The frame is centered at the target. The x-axis is aligned with the primary–secondary direction, the z-axis is normal to the primary–secondary plane in the direction of their angular momentum, and the y-axis completes the dextral orthonormal triad. ICs are defined in this frame [31].

2.2.2 Ephemerides

Precise states of the Sun and major planets are retrieved from the Jet Propulsion Laboratory (JPL)'s planetary ephemerides `de440s.bsp`[1] (or DE440s) [42]. Additionally, the ephemerides `mars097.bsp` of Mars (the target) and its moons are employed[2]. The following generic leap seconds kernel (LSK) and planetary constants kernel (PCK) are used: `naif0012.tls`, `pck00010.tpc`, and `gm_de432.tpc`[3].

[1]Data publicly available at: `https://naif.jpl.nasa.gov/pub/naif/generic_kernels/spk/planets/de440s.bsp` [retrieved Sep 2, 2022].

[2]`~/spk/satellites/mars097.bsp` [retrieved Sep 2, 2022].

[3]Data publicly available at: `https://naif.jpl.nasa.gov/pub/naif/generic_kernels/lsk/naif0012.tls`, and `~/generic_kernels/pck/pck00010.tpc` [retrieved Sep 2, 2022]. The `gm_de440.tpc` PCK kernel was written from scratch, courtesy of Dr. C. Giordano, because the new version consistent with ephemerides DE440s has not been released yet.

Table 1: Assumed spacecraft specifications.

Specification	Symbol	Value
Mass	m	$24\,\mathrm{kg}$
SRP area	A	$0.32\,\mathrm{m}^2$
Coefficient of reflectivity	C_r	1.3

2.2.3 Equations of motion

The equations of motion (EoM) used are those of the restricted N-body problem. The gravitational attractions of the Sun, Mercury, Venus, Earth (B[4]), Mars (central body), Jupiter (B), and Saturn (B) are considered. Additionally, solar radiation pressure (SRP) is also included and implemented as a *cannonball* (or *spherical*) model [43]. The assumed spacecraft specifications needed to evaluate the SRP perturbation are collected in Table 1. They are compatible with the specifications of a 12U deep-space CubeSat [44].

The EoM, written in a non-rotating Mars-centered reference frame, are [6, 30]

$$\ddot{\mathbf{r}} = -\frac{\mu_t}{r^3}\mathbf{r} - \sum_{i\in\mathbb{P}}\mu_i\left(\frac{\mathbf{r}_i}{r_i^3} + \frac{\mathbf{r}-\mathbf{r}_i}{\|\mathbf{r}-\mathbf{r}_i\|^3}\right) + \frac{QA}{m}\frac{\mathbf{r}-\mathbf{r}_\odot}{\|\mathbf{r}-\mathbf{r}_\odot\|^3} \quad (1)$$

where μ_t is the gravitational parameter of the target body; $\mathbf{r}$ is the position vector of the spacecraft with respect to the target and r is its magnitude; $\mathbb{P}$ is a set of $N-2$ indexes each referring to a perturbing body; μ_i and $\mathbf{r}_i$ are the gravitational parameter and position vector with respect to the target of the ith body, respectively; A is the Sun-projected area on the spacecraft for SRP evaluation; m is the spacecraft mass; $\mathbf{r}_\odot$ is the position vector of the Sun with respect to the target. Lastly, $Q = \frac{LC_r}{4\pi c}$, where C_r is the spacecraft reflectivity coefficient, $c = 299\,792\,458\,\mathrm{m\,s^{-1}}$ is the speed of light in vacuum from SPICE [45, 46], and $L = S_\odot 4\pi d_{\mathrm{AU}}^2$ is the Sun luminosity computed from the solar constant[5] $S_\odot = 1367.5\,\mathrm{W\,m^{-2}}$ evaluated at $d_{\mathrm{AU}} = 149\,597\,870\,613.6889\,\mathrm{m} = 1\,\mathrm{AU}$.

2.2.4 Numerical integration of the EoM

[30]. Nondimensionalization units are reported in Table 2. For point-wise simulations, the numerical integration is carried with the DOPRI8 propagation scheme [47]. It is an adaptive step, 8th-order Runge–Kutta integrator with 7th-order error control, the coefficients were derived by Prince and Dormand [48]. The dynamics are propagated setting the relative tolerance to 10^{-12} [30].

[4]Here B stands for barycenter.

[5]`https://extapps.ksc.nasa.gov/Reliability/Documents/Preferred_Practices/2301.pdf` [last accessed Sep 2, 2022].

Table 2: Nondimensionalization units.

Unit	Symbol	Value	Comment
Gravity parameter	MU	$42\,828.376\,\mathrm{km}^3\,\mathrm{s}^{-2}$	Mars' gravity parameter μ_t
Length	LU	$3396.0000\,\mathrm{km}$	Mars' radius $R_{\male}$
Time	TU	$956.281\,42\,\mathrm{s}$	$(\mathrm{LU}^3/\mathrm{MU})^{0.5}$
Velocity	VU	$3.551\,255\,8\,\mathrm{km\,s}^{-1}$	LU/TU

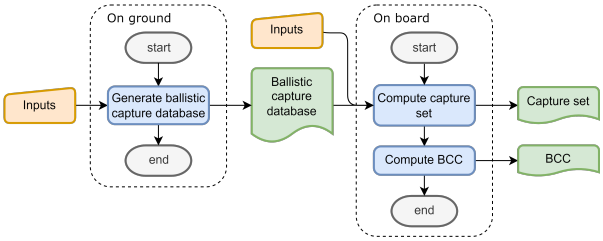

Figure 1: ABC algorithm flowchart.

3 Methodology

Present-day approaches to search for BC orbits are computationally demanding. They are not suitable for onboard implementation, this applies especially to the case of autonomous spacecraft with limited resources. In this work, we introduce an ABC algorithm tailored for spacecraft with reduced computational capability and that could potentially see the implementation onboard of interplanetary autonomous CubeSat. An overview about the ABC algorithm and the details on how to tackle the problem of generating new capture orbits directly onboard of CubeSats are provided in what follows.

3.1 ABC algorithm

The flowchart in Figure 1 gives and overview of the ABC algorithm. The algorithm is composed by two major segments. The first is carried out on ground and aims to prepare a ballistic capture corridor (BCC) database [6] that is necessary for the second part of the procedure. The second segment is carried out on board and foresees the CubeSat (or a spacecraft in general) computing new BC sets from which desired BCCs are developed [6]. The onboard computation of new capture sets at succeeding capture epochs is made possible by solving a sequence of 3PBVPs. Starting from the IC of a known BC orbit, the state is sequentially corrected both in forward and backward times to derive the ICs of new orbits at the desired capture epochs. The new solutions exhibit the same qualitative dynamical behavior and are similar in shape to the original capture orbit but they are shifted in time. To be successful, the method requires as starting point an enough regular baseline capture orbit.

3.2 Problem statement

Provided that an enough regular BC orbit is known, then the primary goal of the ABC algorithm is to derive a modified IC at a desired capture epoch that retains the dynamical behavior of the original BC orbit. This means that the known reference IC $(\hat{\mathbf{x}}_0, \hat{t}_0) \in \mathcal{C}^n_{-1}$ is corrected into a new IC $(\mathbf{x}_0, t_0) \in \mathcal{C}^n_{-1}$. The related orbits are defined as follows:

Definition. *Let $(\mathbf{x}_0, t_0) \in \mathbb{R}^6 \times \mathbb{R}$ and $\boldsymbol{\varphi}(\mathbf{x}_0, t_0; t)$ be the starting point and the solution at time t, respectively, of the Cauchy problem*

$$\begin{cases} \dot{\mathbf{x}} = \mathbf{f}(\mathbf{x}, t) \\ \mathbf{x}(t_0) = \mathbf{x}_0 \end{cases}, \tag{2}$$

then the related trajectory γ is defined as

$$\gamma(\mathbf{x}_0, t_0) := \{\boldsymbol{\varphi}(\mathbf{x}_0, t_0; t) \ \forall \ t \in \mathbb{R}\}. \tag{3}$$

In Equation (2), the first relation is the state space representation of the EoM in Equation (1). Under such dynamics, the orbits $\gamma(\hat{\mathbf{x}}_0, \hat{t}_0)$ and $\gamma(\mathbf{x}_0, t_0)$ are necessarily different because the problem is non-autonomous and $\delta t_0 = t_0 - \hat{t}_0 \neq 0$. Throughout the manuscript, $\gamma(\hat{\mathbf{x}}_0, \hat{t}_0)$ and $(\hat{\mathbf{x}}_0, \hat{t}_0)$ are also referred to as reference BC orbit and IC, respectively. On the other hand, $\gamma(\mathbf{x}_0, t_0)$ and $(\mathbf{x}_0, t_0)$ are indicated as corrected or new BC orbit and IC, respectively. In mathematical terms, our problem can be thus stated as follows:

Problem. *Find a modified initial condition $\mathbf{x}_0$ at a given time t_0 such that $\gamma(\mathbf{x}_0, t_0)$ retains the dynamical behavior of $\gamma(\hat{\mathbf{x}}_0, \hat{t}_0)$. In particular, if $(\hat{\mathbf{x}}_0, \hat{t}_0) \in \mathcal{C}^n_{-1}$ and $\gamma(\hat{\mathbf{x}}_0, \hat{t}_0)$ is a ballistic capture orbit, then $\hat{\mathbf{x}}_0$ shall be corrected into $\mathbf{x}_0$ such that $(\mathbf{x}_0, t_0) \in \mathcal{C}^n_{-1}$ and $\gamma(\mathbf{x}_0, t_0)$ is a ballistic capture orbit.*

The methodology devised to tackle this problem envisages five steps:

1. expansion of the flow $\boldsymbol{\varphi}(\mathbf{x}_0, t_0; t_f)$ about the reference solution $\gamma(\hat{\mathbf{x}}_0, \hat{t}_0)$ at final forward time $t_f > t_0$, after the particle has performed n revolutions about the target, so satisfying condition $(\mathbf{x}_0, t_0) \in \mathcal{W}_n$;
2. expansion of the flow $\boldsymbol{\varphi}(\mathbf{x}_0, t_0; t_b)$ about the reference solution $\gamma(\hat{\mathbf{x}}_0, \hat{t}_0)$ at final backward time

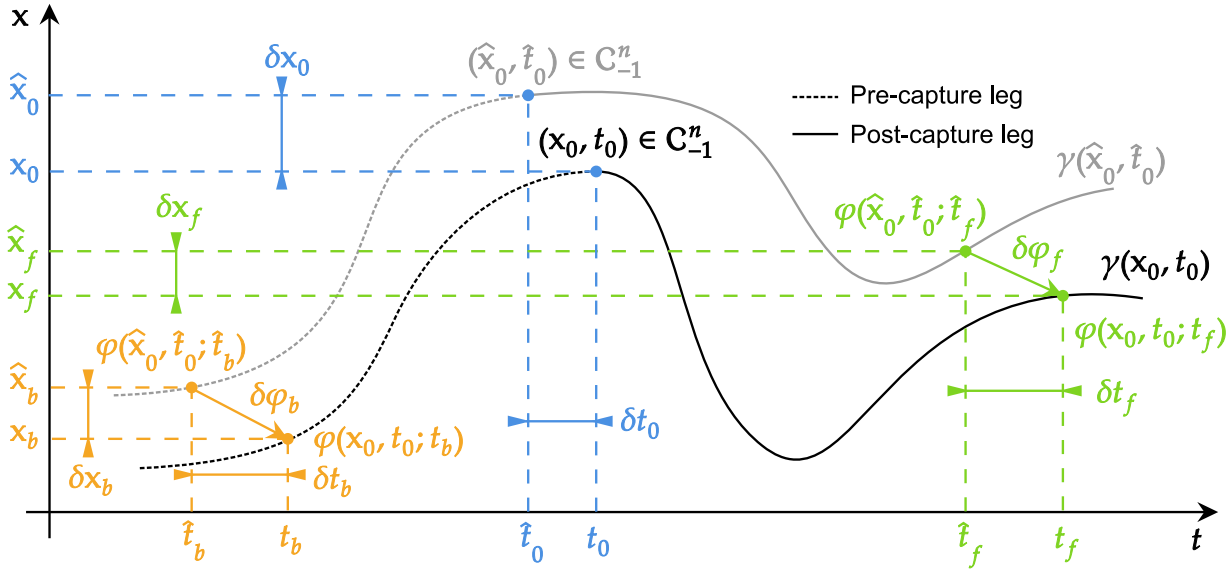

Figure 2: Representation of flow expansion.

$t_b < t_0$, when the particle escapes from the target, so satisfying condition $(\mathbf{x}_0, t_0) \in \mathcal{X}_{-1}$;

3. specification of enough boundary conditions to well-pose the 3PBVP [49];
4. linearization of nonlinear boundary conditions;
5. solution of the 3PBVP through multiple shooting.

This is the core part of a larger algorithm where a number N_p of 3PBVPs are solved in sequence to compute a new family of BC orbits at subsequent capture epochs. Provided that the time step δt_0 is small enough, the new BC orbit $\gamma(\mathbf{x}_0, t_0)$ is expected to be similar to the reference one. Consequently, the boundary conditions can be linearized about the reference BC orbit $\gamma(\hat{\mathbf{x}}_0, \hat{t}_0)$. This linearization is beneficial for two reasons: i) it makes boundary conditions consistent with the flow expansion; ii) the problem becomes completely linear, so solving the 3PBVP requires just a matrix inversion.

The notation used throughout the manuscript is herewith introduced. A 3-dimensional vector is indicated as $\mathbf{a} = [a\ b\ c]^\top$, its magnitude as $a = \|\mathbf{a}\|$. Reference quantities are written with a hat as $\hat{\mathbf{a}}$, and the following relation holds $\mathbf{a} = \hat{\mathbf{a}} + \delta\mathbf{a}$. The position vector is $\mathbf{r} = [x\ y\ z]^\top$, the velocity vector is $\mathbf{v} = [\dot{x}\ \dot{y}\ \dot{z}]^\top = [v_x\ v_y\ v_z]^\top$, the state space vector is $\mathbf{x} = \left[\mathbf{r}^\top\ \mathbf{v}^\top\right]^\top$, and the angular momentum is $\mathbf{h} = \mathbf{r} \times \mathbf{v} = [\mathbf{r}^\wedge]\,\mathbf{v}$, where the skew-symmetric matrix $[\mathbf{a}^\wedge]$ is defined as

$$\left[\mathbf{a}^\wedge\right] := \begin{bmatrix} 0 & -c & b \\ c & -0 & -a \\ -b & a & 0 \end{bmatrix}. \tag{4}$$

According to previous remarks, $\mathbf{r}_0 = \hat{\mathbf{r}}_0 + \delta\mathbf{r}_0$, $\mathbf{v}_0 = \hat{\mathbf{v}}_0 + \delta\mathbf{v}_0$, and $\mathbf{h}_0 = \hat{\mathbf{h}}_0 + \delta\mathbf{h}_0$. In first approximation, $\delta\mathbf{h} = \mathbf{r} \times \delta\mathbf{v} - \mathbf{v} \times \delta\mathbf{r} = [\mathbf{r}^\wedge]\,\delta\mathbf{v} - [\mathbf{v}^\wedge]\,\delta\mathbf{r}$. Finally, the 20-dimensional vector $\mathbf{z}$ is defined as $\mathbf{z} = \left[\mathbf{x}_0^\top\ \mathbf{x}_f^\top\ \mathbf{x}_b^\top\ t_f\ t_b\right]^\top$.

3.3 Flow expansion

The Taylor expansion truncated at the first order of the flow $\boldsymbol{\varphi}(\mathbf{x}_0, t_0; t_f)$ is

$$\begin{aligned} \boldsymbol{\varphi}(\mathbf{x}_0, t_0; t_f) &= \boldsymbol{\varphi}(\hat{\mathbf{x}}_0 + \delta\mathbf{x}_0, \hat{t}_0 + \delta t_0; \hat{t}_f + \delta t_f) \approx \\ &\approx \boldsymbol{\varphi}(\hat{\mathbf{x}}_0, \hat{t}_0; \hat{t}_f) + \frac{\partial\boldsymbol{\varphi}}{\partial\mathbf{x}_0}\delta\mathbf{x}_0 + \frac{\partial\boldsymbol{\varphi}}{\partial t_0}\delta t_0 + \frac{\partial\boldsymbol{\varphi}}{\partial t_f}\delta t_f \end{aligned} \tag{5}$$

where the partial derivatives are

$$\frac{\partial\boldsymbol{\varphi}}{\partial\mathbf{x}_0} = \boldsymbol{\Phi}(\mathbf{x}_0, t_0; t_f) = \boldsymbol{\Phi}_{t_0}^{t_f}, \tag{6}$$

$$\frac{\partial\boldsymbol{\varphi}}{\partial t_0} = -\boldsymbol{\Phi}_{t_0}^{t_f}\mathbf{f}(\mathbf{x}_f, t_f), \tag{7}$$

$$\frac{\partial\boldsymbol{\varphi}}{\partial t_f} = \mathbf{f}(\mathbf{x}_f, t_f). \tag{8}$$

They are evaluated at $(\hat{\mathbf{x}}_0, \hat{t}_0; \hat{t}_f)$. $\boldsymbol{\Phi}$ is the state transition matrix [50]. The derivative in Equation (7) is computed according to [51]. Hence, the expansion becomes

$$\delta\boldsymbol{\varphi}_f \approx \boldsymbol{\Phi}_{\hat{t}_0}^{\hat{t}_f}\delta\mathbf{x}_0 - \boldsymbol{\Phi}_{\hat{t}_0}^{\hat{t}_f}\mathbf{f}(\hat{\mathbf{x}}_f, \hat{t}_f)\delta t_0 + \mathbf{f}(\hat{\mathbf{x}}_f, \hat{t}_f)\delta t_f \tag{9}$$

where $\delta\boldsymbol{\varphi}_f = \boldsymbol{\varphi}_f - \hat{\boldsymbol{\varphi}}_f = \boldsymbol{\varphi}(\mathbf{x}_0, t_0; t_f) - \boldsymbol{\varphi}(\hat{\mathbf{x}}_0, \hat{t}_0; \hat{t}_f)$. Similarly, the Taylor expansion truncated at the first order of the flow $\boldsymbol{\varphi}(\mathbf{x}_0, t_0; t_b)$ is

$$\delta\boldsymbol{\varphi}_b \approx \boldsymbol{\Phi}_{\hat{t}_0}^{\hat{t}_b}\delta\mathbf{x}_0 - \boldsymbol{\Phi}_{\hat{t}_0}^{\hat{t}_b}\mathbf{f}(\hat{\mathbf{x}}_b, \hat{t}_b)\delta t_0 + \mathbf{f}(\hat{\mathbf{x}}_b, \hat{t}_b)\delta t_b \tag{10}$$

where $\delta\boldsymbol{\varphi}_b = \boldsymbol{\varphi}_b - \hat{\boldsymbol{\varphi}}_b = \boldsymbol{\varphi}(\mathbf{x}_0, t_0; t_b) - \boldsymbol{\varphi}(\hat{\mathbf{x}}_0, \hat{t}_0; \hat{t}_b)$. Overall, Equations (9) and (10) provide 12 relations. Given

$\delta t_0 = t_0 - \hat{t}_0$, 20 terms still remain unknown. They are $\delta\mathbf{x}_0$, $\delta\boldsymbol{\varphi}_f = \delta\mathbf{x}_f$, δt_f, $\delta\boldsymbol{\varphi}_b = \delta\mathbf{x}_b$, and δt_b. Therefore, 8 boundary conditions must be specified to well-pose the problem. To better clarify, Figure 2 proposes a representation of the flow expansion on the $t\mathbf{x}$-plane. For the sake of simplicity, the 6-dimensional state space $\mathbf{x}$ is represented as 1-dimensional in Figure 2.

3.4 Boundary conditions

The necessary 8 boundary conditions are obtained as follows. Firstly, 3 relations (1 vector and 2 scalar equations) are enforced at capture epoch (at initial time t_0). Then, other 3 are imposed after n revolution about the target (at final forward time t_f). Finally, 1 condition is prescribed at the escape (at final backward time t_b). They are individually discussed in the next paragraphs.

Boundary condition $\mathbf{i_0}$) The IC $\mathbf{x}_0$ belongs to a certain orbital plane at t_0 (defined in the RTN@t_0 frame). It is required that the new IC belongs to the same plane but defined at time $t_0 + \delta t_0$. This is to follow Mars in its orbital revolution. In mathematical terms

$$\mathbf{h}_0^{\text{RTN@}(t_0+\delta t_0)} = \hat{\mathbf{h}}_0^{\text{RTN@}t_0}. \tag{11}$$

Linearizing Equation (11), a more compact expression is obtained

$$\mathbf{M}_1\mathbf{z} + \mathbf{b}_1 = \mathbf{0} \tag{12}$$

where only the first 2 rows in Equation (11) are retained because the last relation is not linearly independent.

Boundary condition $\mathbf{ii_0}$) The new IC shall be a pericenter. This is translated into

$$\mathbf{r}_0 \cdot \mathbf{v}_0 = 0, \tag{13}$$

a scalar equation that once linearized gives

$$\mathbf{m}_2^\top \mathbf{z} + b_2 = 0. \tag{14}$$

Boundary condition $\mathbf{iii_0}$) The new IC is enforced to have osculating orbital elements with eccentricity $e_0 = \hat{e}_0$, so meaning $\delta e_0 = 0$. Since $\theta_0 = 0$, that is done exploiting the two-body problem orbit equation

$$\|\mathbf{r}_0\| = \frac{\mathbf{h}_0 \cdot \mathbf{h}_0}{\mu_t(1+e_0)} = \frac{\mathbf{h}_0 \cdot \mathbf{h}_0}{\mu_t(1+\hat{e}_0)}. \tag{15}$$

Once linearized, it provides the following scalar relation

$$\mathbf{m}_3^\top \mathbf{z} + b_3 = 0. \tag{16}$$

Boundary condition $\mathbf{i_f}$) The final state shall perform the nth revolution about the central body. Mathematically, that is translated into

$$\mathbf{r}_f \cdot \mathbf{v}_0 = 0. \tag{17}$$

As it is written, the boundary condition only enforces that a revolution is completed at epoch t_f. Consequently, the boundary condition cannot assure that exactly n revolutions are performed. However, the correct number of revolutions is achieved because the new solution is expected to be similar to the reference one for small enough δt_0. After linearization, the boundary condition becomes

$$\mathbf{m}_4^\top \mathbf{z} + b_4 = 0. \tag{18}$$

Boundary condition $\mathbf{ii_f}$) The Keplerian energy at final forward time of the new ballistic capture orbit shall be equal to the final Keplerian energy of the reference final state. This is enforced to preserve capture in forward time, that is $(\mathbf{x}_0, t_0) \in \mathcal{W}_n$. The scalar condition reads

$$\frac{\mathbf{v}_f \cdot \mathbf{v}_f}{2} - \frac{\mu_t}{\|\mathbf{r}_f\|} = \frac{\hat{\mathbf{v}}_f \cdot \hat{\mathbf{v}}_f}{2} - \frac{\mu_t}{\|\hat{\mathbf{r}}_f\|}, \tag{19}$$

then linearized as

$$\mathbf{m}_5^\top \mathbf{z} + b_5 = 0. \tag{20}$$

Boundary condition $\mathbf{iii_f}$) The variation on the final eccentricity magnitude $e_f = \hat{e}_f + \delta e_f$ shall be null, then $\delta e_f = 0$. Hence, the condition can be written as

$$\mathbf{e}_f \cdot \mathbf{e}_f = \hat{\mathbf{e}}_f \cdot \hat{\mathbf{e}}_f. \tag{21}$$

Substituting $\mathbf{e} = \dfrac{\mathbf{v}\times\mathbf{h}}{\mu_t} - \dfrac{\mathbf{r}}{r}$ and linearizing, the following expression is derived

$$\mathbf{m}_7^\top \mathbf{z} + b_7 = 0. \tag{22}$$

Boundary condition $\mathbf{i_b}$) The Keplerian energy at the final backward time of the new ballistic capture orbit shall be equal to the final Keplerian energy of reference final state. This is enforced to preserve escape in backward time, which means $(\mathbf{x}_0, t_0) \in \mathcal{X}_{-1}$. Similarly to Equation (19), the condition is expressed as

$$\frac{\mathbf{v}_b \cdot \mathbf{v}_b}{2} - \frac{\mu_t}{\|\mathbf{r}_b\|} = \frac{\hat{\mathbf{v}}_b \cdot \hat{\mathbf{v}}_b}{2} - \frac{\mu_t}{\|\hat{\mathbf{r}}_b\|}, \tag{23}$$

and once linearized reads

$$\mathbf{m}_6^\top \mathbf{z} + b_6 = 0. \tag{24}$$

3.5 3PBVP solved through multiple shooting

A 3PBVP [53, 54] consists in finding $\mathbf{x}_0$, $t \in [t_b, t_f]$ with $t_b \leq t_0 \leq t_f$, such that

$$\dot{\mathbf{x}} = \mathbf{f}(\mathbf{x}, t), \quad \mathbf{g}(\mathbf{x}(t_b), \mathbf{x}(t_0), \mathbf{x}(t_f)) = \mathbf{0}. \tag{25}$$

The first equation is the state space representation of Equation (1), while function $\mathbf{g}$ specifies eight boundary conditions needed to well-pose the problem [49]. According to the multiple shooting approach, the problem presented in Equation (25) can be solved for a finite set of variables [54, 55].

In multiple shooting, the solution is discretized over m and l grid points in forward and backward time, respectively. In forward time, the discretization is $t0 < t_1 < \cdots < t_{m-1} = t_f$, so meaning $\mathbf{s}_j = \mathbf{x}(t_j) = \mathbf{x}_j$ with $j = 1, 2, \ldots, m-1$. In backward time, it is $t_b = t_{1-l} < \cdots < t_{-1} < t_0$, that is $\mathbf{s}_k = \mathbf{x}(t_k) = \mathbf{x}_k$ with $k = -1, -2, \ldots, 1-l$. The discretized solution at initial time is $\mathbf{s}_0 = \mathbf{x}(t_0) = \mathbf{x}_0$, the one at final forward time is $\mathbf{s}_{m-1} = \mathbf{x}(t_f) = \mathbf{x}_f$, and that at final backward time is $\mathbf{s}_{1-l} = \mathbf{x}(t_b) = \mathbf{x}_b$. Consequently, $m-1$ and $l-1$ segments are defined in forward and backward time, respectively, in which a 3PBVP is solved by enforcing continuity of the solutions at both ends. The advantage of the multiple shooting is to reduce sensitivity by shortening the duration of the original problem. The defect vectors are

$$\begin{aligned} \boldsymbol{\zeta}_j &= \boldsymbol{\varphi}(\mathbf{s}_{j-1}, t_{j-1}; t_j) - \mathbf{s}_j, \quad t_j = t_0 + j\frac{t_{m-1} - t_0}{m-1}, \\ \boldsymbol{\zeta}_k &= \boldsymbol{\varphi}(\mathbf{s}_{k+1}, t_{k+1}; t_k) - \mathbf{s}_k, \quad t_k = t_0 - k\frac{t_{1-l} - t_0}{l-1}, \end{aligned} \tag{26}$$

with $j = 1, \ldots, m-1$ and $k = -1, \ldots, 1-l$. The defects $\boldsymbol{\zeta}_j = \boldsymbol{\zeta}_j(\mathbf{s}_{j-1}, \mathbf{s}_j, t_{m-1})$ and $\boldsymbol{\zeta}_k = \boldsymbol{\zeta}_k(\mathbf{s}_{k+1}, \mathbf{s}_k, t_{1-l})$ depend on t_{m-1} and t_{1-l} through the relations in Equation (26) [51]. The new problem is to determine $\mathbf{s}_j$, $\mathbf{s}_k$, $\mathbf{s}_0$, t_{m-1}, and t_{1-l} such that

$$\begin{aligned} &\mathbf{g}(\mathbf{s}_0, \mathbf{s}_{m-1}, \mathbf{s}_{1-l}, t_{m-1}, t_{1-l}) = \mathbf{0}, \\ &\boldsymbol{\zeta}_j = \mathbf{0}, \quad j = 1, \ldots, m-1, \\ &\boldsymbol{\zeta}_k = \mathbf{0}, \quad k = -1, \ldots, 1-l. \end{aligned} \tag{27}$$

In Equation (27), there are $6(m+l-1)+2$ unknowns and $6(m+l-2)+8$ equations (8 boundary conditions and $6(m+l-2)$ defect constraints).

The complete set of 8 linearized boundary conditions form a linear system that in matrix form reads

$$\bar{\mathbf{g}}(\mathbf{z}) = \mathbf{M}\mathbf{z} + \mathbf{b}_m = \mathbf{0} \tag{28}$$

where $\mathbf{z}$ is the variable matrix previously defined in Section 3.2. The coefficient matrix $\mathbf{M}$ and constant matrix $\mathbf{b}_m$ are constructed as follows

$$\mathbf{M} = \begin{bmatrix} \mathbf{M}_1^\top & \mathbf{m}_2 & \mathbf{m}_3 & \mathbf{m}_3 & \mathbf{m}_4 & \mathbf{m}_5 & \mathbf{m}_6 & \mathbf{m}_7 \end{bmatrix}^\top, \tag{29}$$

$$\mathbf{b}_m = \begin{bmatrix} \mathbf{b}_1^\top & b_2 & b_3 & b_4 & b_5 & b_6 & b_7 \end{bmatrix}^\top. \tag{30}$$

Defects $\boldsymbol{\zeta}_j$ and $\boldsymbol{\zeta}_k$ can be expressed in matrix form as

$$\boldsymbol{\zeta} = \mathbf{D}\,\mathbf{s} + \mathbf{b}_d = \mathbf{0}. \tag{31}$$

Eventually, the full system of 6(m+l-2)+8 equations is built by combining Equations (31), and (28). It reads

$$\mathbf{A}\mathbf{s} = \mathbf{b} \tag{32}$$

where the coefficient, variable, and constant matrices are

$$\mathbf{A} = \begin{bmatrix} \mathbf{D} \\ \mathbf{M}_{(:,1:6)} \quad \mathbf{0} \quad \mathbf{M}_{(:,7:12)} \quad \mathbf{0} \quad \mathbf{M}_{(:,13:20)} \end{bmatrix}, \tag{33}$$

$$\mathbf{s} = \begin{bmatrix} \mathbf{s}_0^\top & \mathbf{s}_1^\top & \cdots & \mathbf{s}_{m-1}^\top & \mathbf{s}_{-1}^\top & \cdots & \mathbf{s}_{1-l}^\top & t_{m-1} & t_{1-l} \end{bmatrix}^\top, \tag{34}$$

$$\mathbf{b} = -\begin{bmatrix} \mathbf{b}_d^\top & \mathbf{b}_m^\top \end{bmatrix}^\top. \tag{35}$$

3.6 Generation of BC orbit family

The algorithm to generate a family of BC orbits is herewith discussed. First of all, an enough regular BC orbit $\gamma(\mathbf{x}_0^*, t_0^*) \in \mathcal{C}_{-1}^n$ is chosen. Such orbit is referred to as baseline and it is used as seed to generate the whole family of new BC orbits. Then, the desired number of revolutions n, the desired capture epoch increment δt_0, and the desired sequence length in terms of steps number N_p are defined. If $\delta t_0 > 0$ (< 0), then the family is built in forward (backward) time. Before solving the sequence of 3PBVPs, the baseline starting point $(\mathbf{x}_0^*, t_0^*)$ is checked to grant capture and belong to $\mathcal{C}_{-1}^n$.

Next, the sequence of 3PBVPs is solved. The number of forward points m is set equal to the number of revolutions n about the target plus 1. In this way, the number of forward segments equals the revolutions. The number of backward points l is set equal to 2, such that the escape leg is fully covered in one segment. Later, a loop iterating from 1 to N_p is performed. In the first iteration, the reference solution is set equal to the baseline one. For each iteration, the new capture epoch is updated to $t_0 = \hat{t}_0 + \delta t_0$, and the coefficient matrix $\mathbf{A}$ and constant matrix $\mathbf{b}$ are computed from the current reference solution $\gamma(\hat{\mathbf{x}}_0, \hat{t}_0)$. The linear system in Equation (32) is solved, and the new BC IC $(\mathbf{x}_0, t_0)$ is extracted from the variable $\mathbf{s}$. The set of nonlinear boundary conditions i_0), ii_0), ii_0) are enforced on $(\mathbf{x}_0, t_0)$. This is suggested because boundary conditions may not be exactly satisfied due to linearization and numerical noise.

If a new BC orbit is found, then results are stored, the current solution becomes the reference one, and the loop proceeds to the next iteration. Conversely, if the methodology fails and the current solution is not a capture orbit, then the loop is stopped. Eventually, results are saved for post-processing. The detailed procedure to generate a family of BC orbits is found in Algorithm 1.

Algorithm 1: Generation of BC orbit family.

Procedure INITIALIZATION
- Define baseline capture epoch t_0^*;
- Define baseline BC orbit IC $\mathbf{x}_0^*$;
- Define revolutions number n of capture set $\mathcal{C}_{-1}^n$;
- Define capture epoch increment δt_0; ▷ `if` $\delta t_0 > 0$ (< 0) `then forward (backward) generation`
- Define 3PBVPs sequence number of steps N_p;

Procedure COMPUTE FIRST BC ORBIT
- Solve BC problem for $(\mathbf{x}_0^*, t_0^*)$ based on WSB algorithmic definition [30]; ▷ `done with GRATIS [52]`
- **If** $(\mathbf{x}_0^*, t_0^*) \notin \mathcal{C}_{-1}^n$ ▷ `baseline IC` $(\mathbf{x}_0^*, t_0^*)$ `not suitable, not a BC orbit`
  - Return;
- **End**

Procedure SOLVE SEQUENCE OF 3PBVPS
- Set number of forward points $m = n + 1$; ▷ `a segment for each revolution`
- Set number of backward points $l = 2$; ▷ `only 1 segment for escape leg`
- Set reference starting point $(\hat{\mathbf{x}}_0, \hat{t}_0) = (\mathbf{x}_0^*, t_0^*)$;
- **While** $i \leq N_p$
  - Update new capture epoch $t_0 = \hat{t}_0 + \delta t_0$;
  - Build matrix $\mathbf{M}$ and vector $\mathbf{b}_m$ of linearized boundary conditions $\bar{\mathbf{g}}(\mathbf{z}) = \mathbf{0}$; ▷ `see Equation` (28)
  - Build matrix $\mathbf{D}$ and vector $\mathbf{b}_d$ of defects constraints $\boldsymbol{\zeta}(\mathbf{s}) = \mathbf{0}$; ▷ `see Equation` (31)
  - Build matrix $\mathbf{A}$ and vector $\mathbf{b}$ of multiple shooting; ▷ `see Equation` (32)
  - Solve linear system $\mathbf{As} = \mathbf{b}$ for variable $\mathbf{s}$;
  - Extract $(\mathbf{x}_0, t_0)$ from variable vector $\mathbf{s}$;
  - Enforce boundary conditions i_0), ii_0), ii_0) on $(\mathbf{x}_0, t_0)$; ▷ `see Equations` (11), (13), `and` (15)
  - Solve BC problem for $(\mathbf{x}_0, t_0)$ based on WSB algorithmic definition [30]; ▷ `done with GRATIS [52]`
  - **If** $(\mathbf{x}_0, t_0) \in \mathcal{C}_{-1}^n$ ▷ `found new BC orbit, 3PBVP solved successfully`
    - Store results $(\mathbf{x}_0^{(i)}, t_0^{(i)}) = (\mathbf{x}_0, t_0)$;
    - Update reference capture epoch $\hat{t}_0 = t_0$;
    - Update reference BC orbit IC $\hat{\mathbf{x}}_0 = \mathbf{x}_0$;
    - Increment loop counter $i = i + 1$;
  - **Else** ▷ `failed to solve current 3PBVP`
    - Save number of new orbits computed $N_{\mathrm{BC}} = i - 1$;
    - Break the loop;
  - **End**
- **End**
- Save results;

Exit

Result: Family of new BC orbits having ICs $(\mathbf{x}_0^{(i)}, t_0^{(i)})$ $\forall\, i = 1, 2, \ldots, N_{\mathrm{BC}}$.

4 Results

The methodology presented in Section 3 is now applied to build two families of BC orbits. The first is a family of orbits belonging to $\mathcal{C}_{-1}^1$ while the second to $\mathcal{C}_{-1}^6$. The families have been built starting from the same baseline capture orbit. The procedure in Algorithm 1 is carried out twice per family, firstly in forward and then in backward direction. The two resulting families have been unified to make a unique, larger family with two branches stemming from the baseline capture orbit $\gamma(\mathbf{x}_0^*, t_0^*)$.

4.1 Baseline BC orbit

The baseline BC sets $\mathcal{C}_{-1}^1$ and $\mathcal{C}_{-1}^6$ are defined in the Mars-centered RTN frame at baseline capture epoch $t_0^* = 0$ days set to 09 DEC 2023 12:00:00.00 (UTC). At that epoch, Mars's true anomaly with respect to the Sun is approximately equal to 270 deg, maximizing $\mathcal{R}_c$ [31]. The selected plane is defined by inclination $i_0^* = 0\,\mathrm{deg}$, and right ascension of the ascending node $\Omega_0^* = 0\,\mathrm{deg}$. Sought trajectories have osculating eccentricity $e_0^* = 0.99$ [13], and true anomaly $\theta_0^* = 0\,\mathrm{deg}$ at the initial epoch t_0^*. If $R_{\male}$ is the radius of Mars in km, then the search space on the plane defined above is a circular crown centered at Mars, from radius $R_{\male} + 100\,\mathrm{km}$ up to radius $10R_{\male}$. Hence, $(r_{p0}^*, \omega_0^*) \in \left[R_{\male} + 100\,\mathrm{km}, 10R_{\male}\right] \times (0, 360]\,\mathrm{deg}$ with r_{p0}^* the pericenter radius, ω_0^* the argument of the pericenter, and grid size set to $[339 \times 360]$.

The baseline BC orbit has been chosen based on

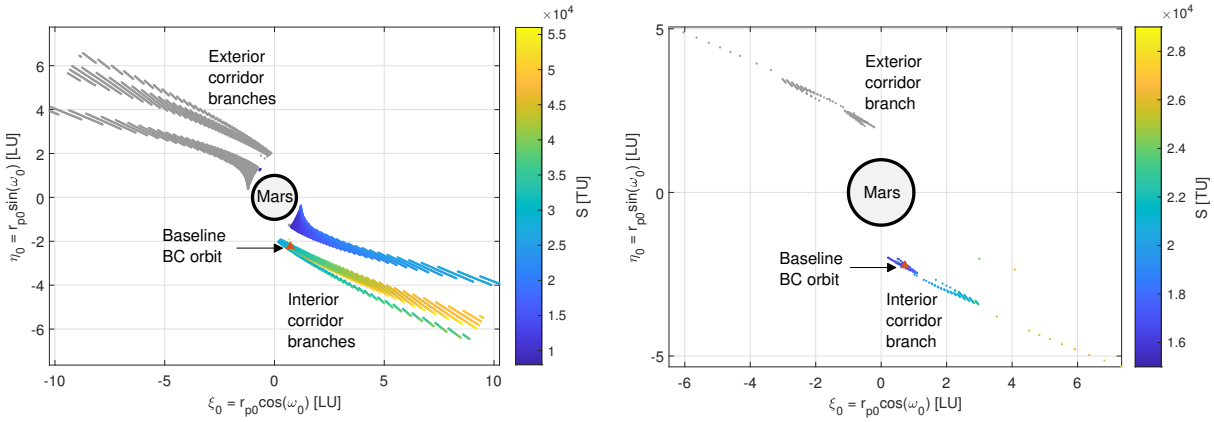

Figure 3: Capture sets at epoch $t_0^* = 0$ days set to 09 DEC 2023 12:00:00.00 (UTC). Regularity index S of branches developing the interior BCC. In gray, branches developing the exterior BCC. Nondimensional coordinates on the orbital plane $i_0^* = \Omega_0^* = 0\,\text{deg}$ defined in the Mars-centered RTN@t_0^* frame. Selected baseline capture orbit marked with red triangle. *Left*: Capture set $\mathcal{C}_{-1}^1$. *Right*: Capture set $\mathcal{C}_{-1}^6$.

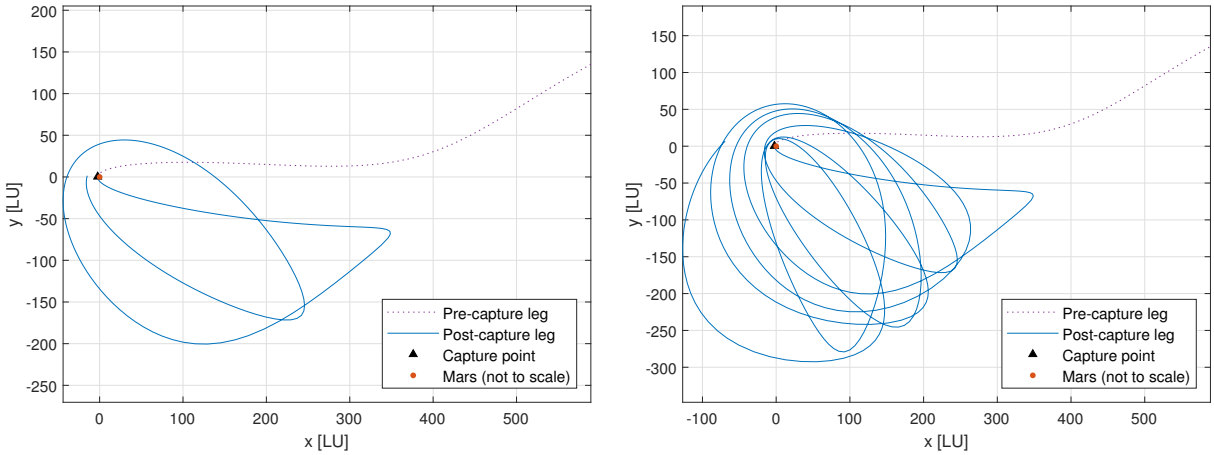

Figure 4: Baseline BC orbit at capture epoch $t_0^* = 0$ days set to 09 DEC 2023 12:00:00.00 (UTC). Pre-capture and post-capture legs represented as purple dotted and blue solid lines, respectively. Nondimensional coordinates in the Mars-centered ECLIPJ2000 frame, xy-plane views. Out of plane motion small but not null. *Left*: Capture orbit $\mathcal{C}_{-1}^1$. *Right*: Capture orbit $\mathcal{C}_{-1}^6$.

its regularity. By visual inspection of capture sets $\mathcal{C}_{-1}^1$ and $\mathcal{C}_{-1}^6$ plots, a regular orbit (small regularity index S) present in both sets has been selected. Such plots are shown in Figure 3, where interior and exterior corridor branches are highlighted too [6]. The baseline BC orbit is marked with a red triangle and has coordinates $(r_{p0}^*, \omega_0^*) = (2.35R_{\male}, 288\,\text{deg})$. The baseline capture orbit is presented in Figure 4. The two orbits shown are propagated starting from the same IC, however their number of revolutions is different. In the chart on the left, the post-capture leg is limited to the 1st revolution. Differently, the post-capture leg of the orbit represented on the right goes on up to the 6th revolution. EoM are written in the 3-dimensional space, however only the xy-plane is shown in Figure 3 and no clues are provided about the out of plane motion. This is done for visualization purposes. Indeed, the out of plane motion is small (but not null) in the ECLIPJ2000 frame and top-views allow a better understanding of the particle motion. The remark applies also to the next plots.

4.2 Families of BC orbits

The family of BC orbits belonging to $\mathcal{C}_{-1}^1$ has been constructed setting $n = 1$, $\delta t_0 = \pm 5$ days, and $N_p = 30$. On the other hand, the family of orbits belonging to $\mathcal{C}_{-1}^6$ has been constructed setting $n = 6$, $\delta t_0 = \pm 2$ days, and $N_p = 75$. The time step of family $\mathcal{C}_{-1}^6$ is smaller compared to family $\mathcal{C}_{-1}^6$ because of the greater difficulty for the algorithm in completing the sequences of 3PBVPs

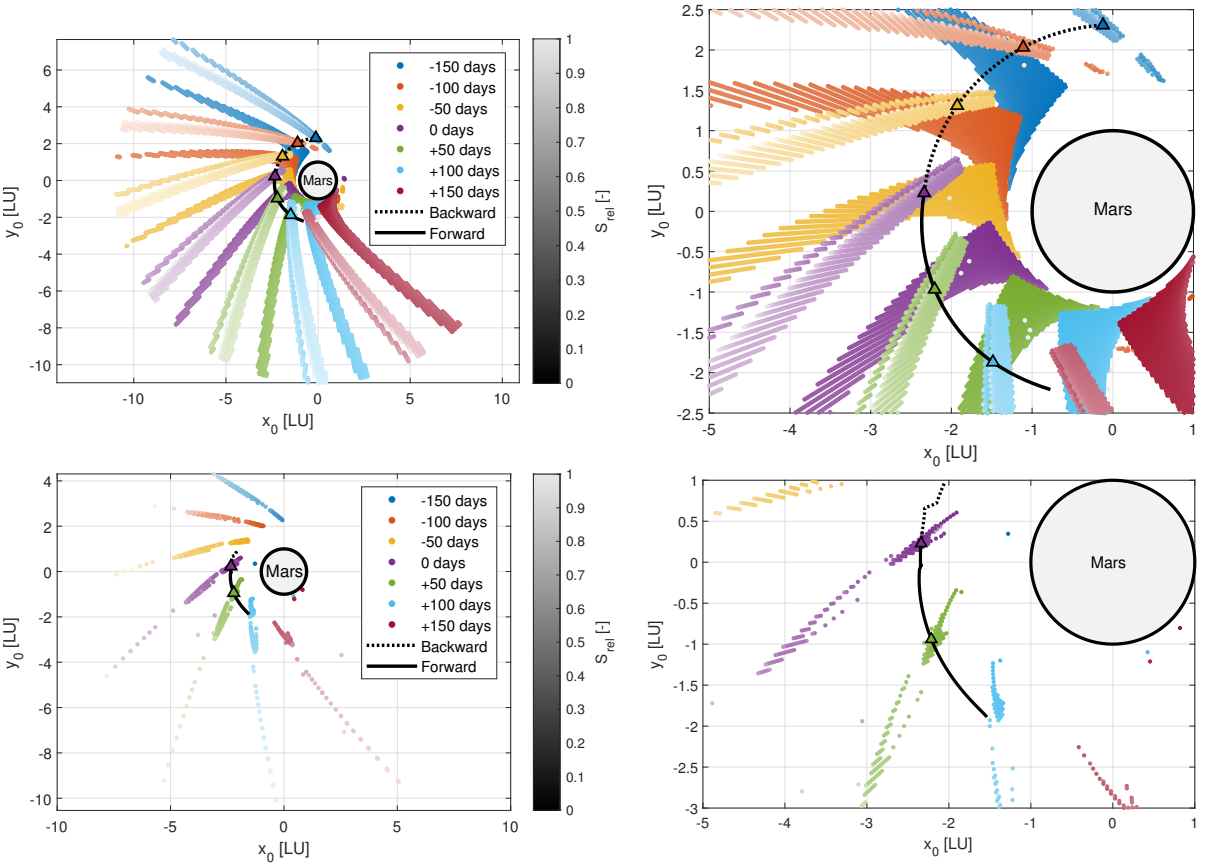

Figure 5: Families of BC orbits generated with Algorithm 1. The black solid and dotted lines represents the forward and backward sequences, respectively. Families overlapped on a collection of capture set branches developing the interior BCC and spanning from $t_0^* - 150$ up to $t_0^* + 150$ days. Baseline capture epoch $t_0^* = 0$ set to 09 DEC 2023 12:00:00.00 (UTC). Triangles mark peculiar BC solutions computed at the same epochs of the visualized capture sets. Correspondence depicted through color code. Regularity index S expressed through color shading. Nondimensional coordinates in the Mars-centered ECLIPJ2000 frame, xy-plane views. Out of plane contribution small but not null. *Top-left*: Family and capture sets $\mathcal{C}_{-1}^1$. *Top-right*: Magnification $\mathcal{C}_{-1}^1$. *Bottom-left*: Family and capture sets $\mathcal{C}_{-1}^6$. *Bottom-right*: Magnification $\mathcal{C}_{-1}^6$.

as the number of revolutions n increases. In the best case, the algorithm would return two families covering 300 days, from $t_0^* - 150$ to $t_0^* + 150$ days. Algorithm 1 has been applied two times per family, once in forward and once in backward direction. In doing so, two sequences of orbits have been obtained for each distinct family that have been later combined.

Results are shown in Figure 5, where the families of BC orbits are drawn. Forward and backward sequences are represented with black solid and dotted lines, respectively. They are overlapped on a collection of capture set branches developing the interior BCC. The plotted sets span capture epoch from $t_0^* - 150$ days up to $t_0^* + 150$ days. Information about the regularity of solutions is expressed through color shading. A color code is used to highlight the generated orbits (marked with triangles) having the same capture epochs of the reported capture sets. To enhance visualization of the region close to Mars, two magnifications are shown on the right hand side of Figure 5.

About family $\mathcal{C}_{-1}^1$ (plots on the top of Figure 5), the methodology successfully completed 27 steps in the forward direction, so reaching +135 days after the baseline capture epoch t_0^*. In backward direction, the algorithm never failed and completed all 30 steps, so providing solutions up to −150 days, before t_0^*. Overall, the baseline solution has been extended for 285 days. The forward sequence failed in correspondence of the discontinuity located on the edge of the capture set branches characterized by larger regularity indexes (lighter branches).

Regarding family $\mathcal{C}_{-1}^6$ (plots on the bottom of Figure 5), 47 and 16 steps have been successfully completed in the forward and backward directions, respectively. As a result, the algorithm provided solutions for 126 days,

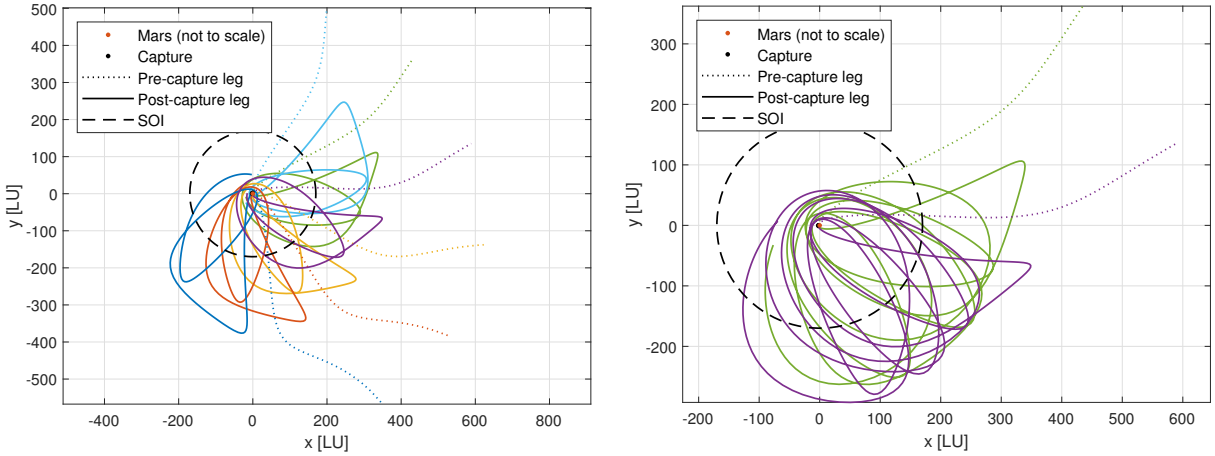

Figure 6: BC orbits at peculiar capture epochs. The color code is that of Figure 5. Pre-capture and post-capture legs represented as dotted and solid lines, respectively. Nondimensional coordinates in the Mars-centered ECLIPJ2000 frame, xy-plane views. Out of plane motion small but not null. *Left*: Orbits family $\mathcal{C}^1_{-1}$. *Right*: Orbits family $\mathcal{C}^6_{-1}$.

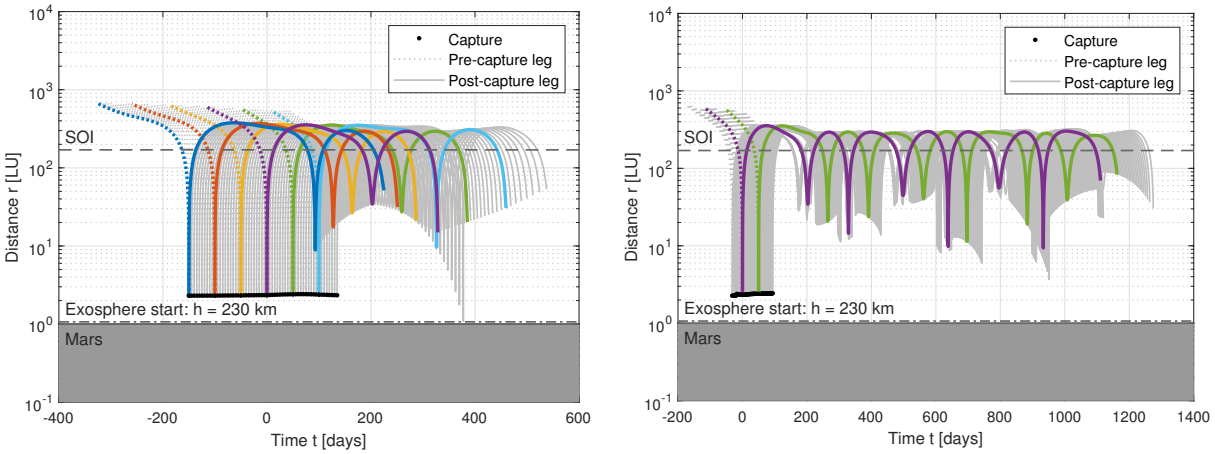

Figure 7: Distance from Mars center of BC orbit families generated with Algorithm 1. Curves colored as corresponding capture orbits shown in Figure 6. The color code is that of Figure 5. Pre-capture and post-capture legs represented as dotted and solid lines, respectively. *Left*: Distances family $\mathcal{C}^1_{-1}$. *Right*: Distances family $\mathcal{C}^6_{-1}$.

up to +94 days in the forward direction and −32 days in the backward one.

The algorithm performed better for family $\mathcal{C}^1_{-1}$ than for family $\mathcal{C}^6_{-1}$, even though a smaller time step δt_0 has been used for the second one. The reason could be found in the shape and size of capture sets. Indeed, sets $\mathcal{C}^1_{-1}$ are wide and dense, while sets $\mathcal{C}^6_{-1}$ are small and sparse. In particular, the sparsity of sets $\mathcal{C}^6_{-1}$ represents and harsh obstacle to vercome for the algorithm, so preventing the successful completion of the full sequence.

Selected BC orbits are plotted in Figure 6. They are the members of the families corresponding to the sets shown in Figure 5. The same color code of Figure 5 applies to Figure 6. As expected, orbits of the same family are really similar in shape. They are rotated about the target due to the revolution of central body about the Sun. The baseline BC orbit is colored in purple and is the same of Figure 4. Mars SOI is also represented for reference, its radius is $R_{\text{SOI}} = 170 R_{♂}$.

The families of BC orbits are now studied in more details. In particular, the distance from the central body and the Keplerian energy are considered of interest. In Figs. 7 and 8, pre-capture and post-capture legs are drawn as dotted and solid lines, respectively. The curves are colored as the corresponding capture orbits shown in Figure 6. The color code is that of Figure 5.

The evolution of distances of the families is presented in Figure 7. As clearly shown by the plots, orbits of both families cross Mars SOI multiple times during the temporary capture. Furthermore, at the escape point, all

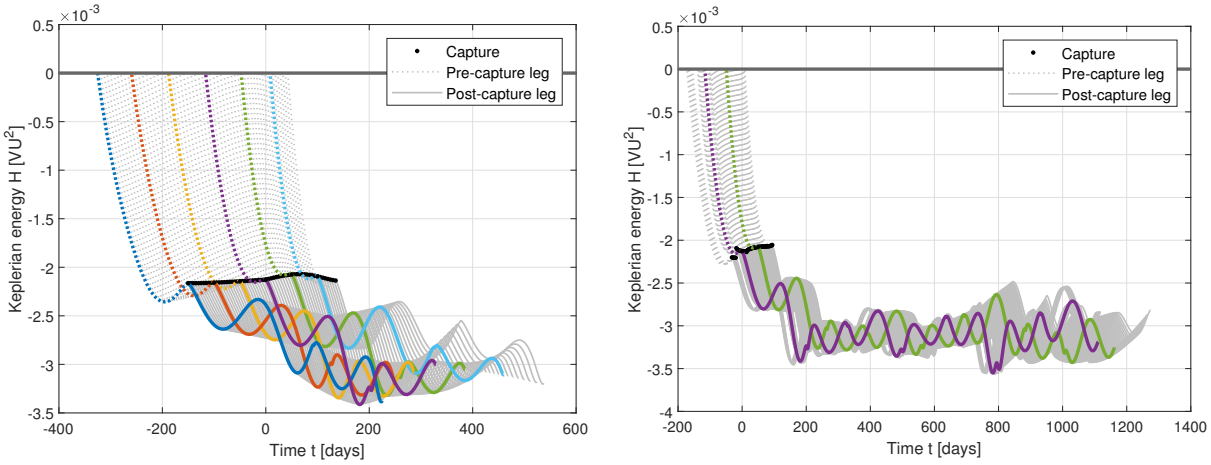

Figure 8: Keplerian energy with respect to Mars of BC orbit families generated with Algorithm 1. Curves colored as corresponding capture orbits shown in Figure 6. The color code is that of Figure 5. Pre-capture and post-capture legs represented as dotted and solid lines, respectively. *Left*: Keplerian energies family $\mathcal{C}^1_{-1}$. *Right*: Keplerian energies family $\mathcal{C}^6_{-1}$.

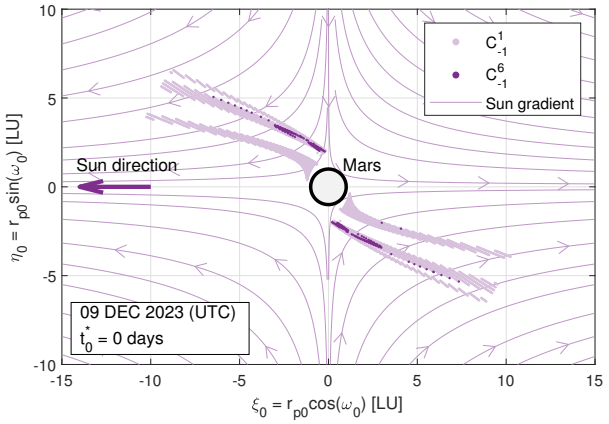

Figure 9: Ballistic capture sets $\mathcal{C}^1_{-1}$ and $\mathcal{C}^6_{-1}$ inspected against the solar gravity gradient. Capture sets and solar gravity gradient computed at baseline capture epoch $t^*_0 = 0$ days set to 09 DEC 2023 12:00:00.00 (UTC). Nondimensional coordinates on the orbital plane $i^*_0 = \Omega^*_0 = 0$ deg defined in the Mars-centered RTN@t^*_0 frame.

orbits have already crossed the SOI, therefore the escape from Mars is always triggered by the zero crossing of the Keplerian energy. Most orbits fly far from Mars surface and all orbits shown in Figure 7 never cross the Exosphere limit located at an altitude of 230 km. However, some solutions fly very close to that limit. Specifically, the ones generated after $t^*_0 + 100$ days, which are those succeeding the light blue curve in left plot of Figure 7. These are orbits whose ICs are close to the previously mentioned discontinuity located near the edge in the less regular (ligther) branches of the capture sets shown in Figure 5. The last orbit of the forward sequence is the one that performs the closest passage to Mars. At the

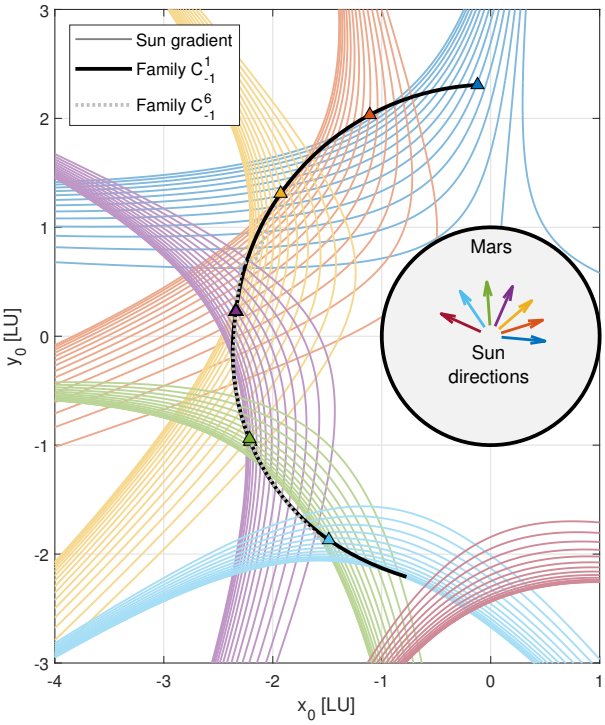

Figure 10: Families $\mathcal{C}^1_{-1}$ and $\mathcal{C}^6_{-1}$ of BC orbits generated with Algorithm 1. Families are inspected against the solar gravity gradient fields computed at peculiar capture epochs spanning from $t^*_0 - 150$ to $t^*_0 + 150$. Baseline capture epoch $t^*_0 = 0$ days set to 09 DEC 2023 12:00:00.00 (UTC). ICs od BC orbits at peculiar epochs marked by triangles. The color code is that of Figure 5. Nondimensional coordinate in the Mars-centered ECLIPJ2000 frame, xy-plane view. Out of plane contribution small but not null.

next step, the algorithm fails because the computed solution falls in the crash set $\mathcal{K}_1$, thus impacting with the target instead of preserving the weakly stable nature of the current reference orbit $\gamma(\hat{\mathbf{x}}_0, \hat{t}_0)$.

The Keplerian energy trend is plotted in Figure 8. As already observed while commenting Figure 7, it is the Keplerian energy that triggers the escapes of all orbits. In fact, the Keplerian energy is always zero at the beginning of all pre-capture legs. Except for some occasional behaviors, the trend of Keplerian energy is quite similar for all the orbits of the same family even though shifted in time. This is akin the observation made on orbit shapes and distances from the target.

4.3 Inspection against solar gravity gradient

To better understand why a reference solution is corrected into a specific new capture orbit according to the methodology described in Section 3, the family of orbits are inspected against the solar gravity gradient. The solar gravity gradient is computed according to [16, 38]. Specifically, the first order Taylor expansion about the origin (corresponding to Mars center) of the Sun gravitational attraction have been evaluated on the domain of interest. The goal of this analysis is to identify some visible patterns or connections to shed some light on why and how the method works.

Figure 9 shows an example of this analysis, where streamlines of the solar gravity gradient are shown on the background of the baseline capture sets $\mathcal{C}^1_{-1}$ and $\mathcal{C}^6_{-1}$. Results are represented in the Mars-centered RTN@t_0^* frame. As a consequence, the Sun direction is aligned with the $-x$ direction. Results match those already reported in the literature.

In Figure 10, the evolution of solar gravity gradient streamlines at peculiar capture epochs are compared against the families of BC orbits. Results are plotted in the Mars-centered ECLIPJ2000 frame. The color code is akin that of Figure 5. Sun directions corresponding to peculiar capture epochs are also reported near the origin of the reference system. Easily recognizable patterns or connections between orbit families and streamlines of the solar gravity gradient are not identified. Consequently, further investigation is necessary to reveal why BC orbit families are constructed along distinctive paths.

5 Conclusion

This work provides and overview of the autonomous ballistic capture algorithm. Specifically, it focuses on the method developed to generate families of ballistic capture orbits having succeeding capture epochs. The fundamental problem of correcting the initial condition of a reference capture orbit, which solution is required for the successful application of the algorithm, has been stated and discussed. The approach to tackle the problem has been explained. Attention has been given to steps including the flow expansion, the definition of the 8 necessary boundary conditions, and their linearization. Then, a three-point boundary value problem has been formulated and solved with the multiple shooting technique. As a result, a linear system has been obtained. Once solved, it provides the initial condition of a new BC orbits. Therefore, families of capture orbits can be easily generated by solving a sequence of linear systems, so reducing the computational burden typically required for finding ballistic capture orbits via usual approaches.

The algorithm has been proven successful in the generation of two families of orbits belonging to capture sets $\mathcal{C}^1_{-1}$ and $\mathcal{C}^6_{-1}$. Based on the results, the algorithm performs better when the revolutions number n is small. For $n = 1$, the method works smoothly and long sequences of BC orbits are built even for large time steps δt_0. Conversely, for many revolutions, the method finds difficult to build long sequences of orbits due to the smallness and sparsity typical of capture sets exhibiting many revolutions about the target. The issue is mitigated by using a small time step δt_0. Nevertheless, the algorithm has been capable of constructing sequences of solutions spanning more than 100 days for both families. Shape, distance, and Keplerian energy of orbits have been studied, proving that the method effectively finds solutions really close to each other, even over large time spans.

The effectiveness in generating wide families of capture orbits, both for few and many revolutions, and the limited computational complexity opens the possibility to the onboard implementation of the algorithm, even for limited platforms like CubeSats. Future work will be focused on developing the remaining parts of the autonomous ballistic capture algorithm, and testing the algorithm firstly in a processor-in-the-loop and then in a hardware-in-the-loop simulation on relevant equipment.

Acknowledgments

G.M. would like to thank the Agenzia Spaziale Italiana (ASI) and the Space Generation Advisory Council (SGAC) for the financial support granted to attend the 20th Space Generation Congress (SGC) and the 73rd International Astronautical Congress (IAC). This work has received funding from the European Research Council (ERC) under the European Union's Horizon 2020 research and innovation programme (Grant Agreement No. 864697).

Bibliography

[1] S Bandyopadhyay, R Foust, G P Subramanian, S-J Chung, and F Y Hadaegh. Review of formation flying and constellation missions using nanosatellites. *Journal of Spacecraft and Rockets*, 53(3):567–578, 2016. DOI: 10.2514/1.a33291.

[2] H Kalita, E Asphaug, S Schwartz, and J Thangavelautham. Network of nano-landers for in-situ characterization of asteroid impact studies. 2017. DOI: arXiv:1709.02885.

[3] A M Hein, M Saidani, and H Tollu. Exploring potential environmental benefits of asteroid mining. In *69th International Astronautical Congress 2018*, 2018. arXiv:1810.04749.

[4] G Di Domenico, E Andreis, A C Morelli, G Merisio, et al. Toward self-driving interplanetary CubeSats: The ERC-funded project EXTREMA. In *72nd International Astronautical Congress*, 2021.

[5] A Morselli, G Di Domenico, E Andreis, A C Morelli, G Merisio, et al. The EXTREMA orbital simulation hub: A facility for GNC testing of autonomous interplanetary CubeSat. In *4S Symposium*, pages 1–13, 2022.

[6] G Merisio and F Topputo. Characterization of ballistic capture corridors aiming at autonomous ballistic capture at Mars. In *2021 AIAA/AAS Astrodynamics Specialist Conference*, pages 1–21, 2021.

[7] A C Morelli, G Merisio, et al. A convex guidance approach to target ballistic capture corridors at Mars. In *44th AAS Guidance, Navigation and Control Conference*, pages 1–24, 2022.

[8] E Andreis, V Franzese, and F Topputo. Onboard orbit determination for deep-space CubeSats. *Journal of guidance, control, and dynamics*, pages 1–14, 2022. DOI: 10.2514/1.G006294.

[9] E Andreis, P Panicucci, V Franzese, and F Topputo. A robust image processing pipeline for planets line-of-sign extraction for deep-space autonomous Cubesats navigation. In *44th AAS Guidance, Navigation and Control Conference*, pages 1–19, 2022.

[10] E Andreis, V Franzese, and F Topputo. An overview of autonomous optical navigation for deep-space CubeSats. In *72nd International Astronautical Congress (IAC 2021)*, pages 1–11, 2021.

[11] A C Morelli, C Hofmann, and F Topputo. Robust low-thrust trajectory optimization using convex programming and a homotopic approach. *IEEE Transactions on Aerospace and Electronic Systems*, 2021. DOI: 10.1109/TAES.2021.3128869.

[12] A C Morelli, C Hofmann, and F Topputo. A homotopic approach for robust low-thrust trajectory design through convex optimization. In *72nd International Astronautical Congress (IAC 2021)*, pages 1–11, 2021.

[13] F Topputo and E Belbruno. Earth–Mars transfers with ballistic capture. *Celestial Mechanics and Dynamical Astronomy*, 121(4):329–346, 2015. DOI: 10.1007/s10569-015-9605-8.

[14] E A Belbruno and J K Miller. Sun-perturbed Earth-to-moon transfers with ballistic capture. *Journal of Guidance, Control, and Dynamics*, 16(4):770–775, jul 1993. DOI: 10.2514/3.21079.

[15] E Belbruno and J Carrico. Calculation of weak stability boundary ballistic lunar transfer trajectories. In *Astrodynamics Specialist Conference*, page 4142, 2000. DOI: 10.2514/6.2000-4142.

[16] C Circi and P Teofilatto. On the dynamics of weak stability boundary lunar transfers. *Celestial Mechanics and Dynamical Astronomy*, 79(1):41–72, 2001. DOI: 10.1023/A:1011153610564.

[17] E Belbruno. Lunar capture orbits, a method of constructing earth moon trajectories and the lunar GAS mission. In *19th International Electric Propulsion Conference*. American Institute of Aeronautics and Astronautics, may 1987. DOI: 10.2514/6.1987-1054.

[18] E A Belbruno and J Miller. A ballistic lunar capture trajectory for the Japanese spacecraft hiten. Technical report, 1990. IOM 312/904-1731-EAB.

[19] E Belbruno. *Capture Dynamics and Chaotic Motions in Celestial Mechanics*. Princeton University Press, dec 2004. DOI: 10.1515/9780691186436.

[20] F García and G Gómez. A note on weak stability boundaries. *Celestial Mechanics and Dynamical Astronomy*, 97(2):87–100, 2007. DOI: 10.1007/s10569-006-9053-6.

[21] F Topputo and E Belbruno. Computation of weak stability boundaries: Sun–Jupiter system. *Celestial Mechanics and Dynamical Astronomy*, 105(1-3):3, 2009. DOI: 10.1007/s10569-009-9222-5.

[22] P A Sousa Silva and M O Terra. Applicability and dynamical characterization of the associated sets of

the algorithmic weak stability boundary in the lunar sphere of influence. *Celestial Mechanics and Dynamical Astronomy*, 113(2):141–168, 2012. DOI: 10.1007/s10569-012-9409-z.

[23] N Hyeraci and F Topputo. Method to design ballistic capture in the elliptic restricted three-body problem. *Journal of guidance, control, and dynamics*, 33(6):1814–1823, 2010. DOI: 10.2514/1.49263.

[24] F Topputo, E Belbruno, and M Gidea. Resonant motion, ballistic escape, and their applications in astrodynamics. *Advances in Space Research*, 42(8):1318–1329, 2008. DOI: 10.1016/j.asr.2008.01.017.

[25] E Belbruno, F Topputo, and M Gidea. Resonance transitions associated to weak capture in the restricted three-body problem. *Advances in Space Research*, 42(8):1330–1351, 2008. DOI: 10.1016/j.asr.2008.01.018.

[26] E Belbruno, M Gidea, and F Topputo. Weak stability boundary and invariant manifolds. *SIAM Journal on Applied Dynamical Systems*, 9(3):1061–1089, 2010. DOI: 10.1137/090780638.

[27] E Belbruno, M Gidea, and F Topputo. Geometry of weak stability boundaries. *Qualitative Theory of Dynamical Systems*, 12(1):53–66, 2013. DOI: 10.1007/s12346-012-0069-x.

[28] E Belbruno. Relation between solutions of the Schrödinger equation with transitioning resonance solutions of the gravitational three-body problem. *Journal of Physics Communications*, 4(1):015012, jan 2020. DOI: 10.1088/2399-6528/ab693f.

[29] F Topputo, M Vasile, and F Bernelli-Zazzera. Low energy interplanetary transfers exploiting invariant manifolds of the restricted three-body problem. *The Journal of the Astronautical Sciences*, 53(4):353–372, 2005. DOI: 10.1007/BF03546358.

[30] Z-F Luo, F Topputo, F Bernelli Zazzera, and G J Tang. Constructing ballistic capture orbits in the real solar system model. *Celestial Mechanics and Dynamical Astronomy*, 120(4):433–450, 2014. DOI: 10.1007/s10569-014-9580-5.

[31] Z-F Luo and F Topputo. Analysis of ballistic capture in Sun–planet models. *Advances in Space Research*, 56(6):1030–1041, 2015. DOI: 10.1016/j.asr.2015.05.042.

[32] G Haller. A variational theory of hyperbolic Lagrangian coherent structures. *Physica D: Nonlinear Phenomena*, 240(7):574–598, 2011. DOI: 10.1016/j.physd.2010.11.010.

[33] George Haller. Lagrangian coherent structures. *Annual Review of Fluid Mechanics*, 47:137–162, 2015. DOI: 10.1146/annurev-fluid-010313-141322.

[34] A Wittig, P Di Lizia, R Armellin, K Makino, F Bernelli-Zazzera, and M Berz. Propagation of large uncertainty sets in orbital dynamics by automatic domain splitting. *Celestial Mechanics and Dynamical Astronomy*, 122(3):239–261, 2015. DOI: 10.1007/s10569-015-9618-3.

[35] M Manzi and F Topputo. A flow-informed strategy for ballistic capture orbit generation. *Celestial Mechanics and Dynamical Astronomy*, 133(11):1–16, 2021. DOI: 10.1007/s10569-021-10048-2.

[36] T Caleb, G Merisio, P Di Lizia, and F Topputo. Stable sets mapping with taylor differential algebra with application to ballistic capture orbits around Mars. *Celestial Mechanics and Dynamical Astronomy*, 134(5):1–22, 2022. DOI: 10.1007/s10569-022-10090-8.

[37] Z F Luo and F Topputo. Mars orbit insertion via ballistic capture and aerobraking. *Astrodynamics*, 5(2):167–181, 2021. DOI: 10.1007/s42064-020-0095-4.

[38] C Giordano and F Topputo. Aeroballistic capture at Mars: Modeling, optimization, and assessment. *Journal of Spacecraft and Rockets*, pages 1–15, 2022. DOI: 10.2514/1.A35176.

[39] Z F Luo and F Topputo. Capability of satellite-aided ballistic capture. *Communications in Nonlinear Science and Numerical Simulation*, 48:211–223, 2017. DOI: 10.1016/j.cnsns.2016.12.021.

[40] D A Dei Tos, R P Russell, and F Topputo. Survey of Mars ballistic capture trajectories using periodic orbits as generating mechanisms. *Journal of Guidance, Control, and Dynamics*, 41(6):1227–1242, 2018. DOI: 10.2514/1.g003158.

[41] B A Archinal, M F A'Hearn, E Bowell, A Conrad, G J Consolmagno, R Courtin, T Fukushima, D Hestroffer, J L Hilton, G A Krasinsky, et al. Report of the IAU working group on cartographic coordinates and rotational elements: 2009. *Celestial Mechanics and Dynamical Astronomy*, 109(2):101–135, 2011. DOI: 10.1007/s10569-010-9320-4.

[42] R S Park, W M Folkner, J G Williams, and D H Boggs. The jpl planetary and lunar ephemerides DE440 and DE441. *The Astronomical Journal*, 161(3):105, 2021. DOI: 10.3847/1538-3881/abd414.

[43] D Scheeres, A Rosengren, and J McMahon. The dynamics of high area-to-mass ratio objects in earth orbit: The effect of solar radiation pressure. In *Proceedings of the AAS/AIAA Space Flight Mechanics Meeting, number AAS*, pages 11–178, 2011.

[44] F Topputo, Y Wang, C Giordano, V Franzese, H Goldberg, F Perez-Lissi, and R Walker. Envelop of reachable asteroids by M-ARGO CubeSat. *Advances in Space Research*, 67(12):4193–4221, 2021. DOI: 10.1016/j.asr.2021.02.031.

[45] C H Acton Jr. Ancillary data services of NASA's navigation and ancillary information facility. *Planetary and Space Science*, 44(1):65–70, 1996. DOI: 10.1016/0032-0633(95)00107-7.

[46] C Acton, N Bachman, B Semenov, and E Wright. A look towards the future in the handling of space science mission geometry. *Planetary and Space Science*, 150:9–12, 2018. DOI: 10.1016/j.pss.2017.02.013.

[47] O Montenbruck and E Gill. *Satellite Orbits Models, Methods and Applications*. Springer, 2000. DOI: 10.1007/978-3-642-58351-3.

[48] P J Prince and J R Dormand. High order embedded Runge–Kutta formulae. *Journal of computational and applied mathematics*, 7(1):67–75, 1981. DOI: 10.1016/0771-050x(81)90010-3.

[49] A Bolle and C Circi. A hybrid, self-adjusting search algorithm for optimal space trajectory design. *Advances in Space Research*, 50(4):471–488, 2012. DOI: 10.1016/j.asr.2012.04.026.

[50] F Topputo. Fast numerical approximation of invariant manifolds in the circular restricted three-body problem. *Communications in Nonlinear Science and Numerical Simulation*, 32:89–98, 2016. DOI: 10.1016/j.cnsns.2015.08.004.

[51] D A Dei Tos and F Topputo. High-fidelity trajectory optimization with application to saddle-point transfers. *Journal of Guidance, Control, and Dynamics*, 42(6):1343–1352, 2019. DOI: 10.2514/1.g003838.

[52] F Topputo, D A Dei Tos, K V Mani, S Ceccherini, C Giordano, V Franzese, and Y Wang. Trajectory design in high-fidelity models. In *7th International Conference on Astrodynamics Tools and Techniques (ICATT)*, pages 1–9, 2018.

[53] R Armellin and F Topputo. A sixth-order accurate scheme for solving two-point boundary value problems in astrodynamics. *Celestial Mechanics and Dynamical Astronomy*, 96(3):289–309, 2006. DOI: 10.1007/s10569-006-9047-4.

[54] D A Dei Tos and F Topputo. Trajectory refinement of three-body orbits in the real solar system model. *Advances in Space Research*, 59(8):2117–2132, 2017. DOI: 10.1016/j.asr.2017.01.039.

[55] G Mingotti, F Topputo, and F Bernelli-Zazzera. Transfers to distant periodic orbits around the Moon via their invariant manifolds. *Acta Astronautica*, 79:20–32, 2012.